Nanoscale

PAPER

View Article Online
View Journal | View Issue

Fragmentation and exfoliation of 2-dimensional materials: a statistical approach†

Cite this: *Nanoscale*, 2014, **6**, 5926

Konstantinos Kouroupis-Agalou,[ae] Andrea Liscio,[a] Emanuele Treossi,[ab] Luca Ortolani,[c] Vittorio Morandi,[c] Nicola Maria Pugno[dfgh] and Vincenzo Palermo*[ab]

The main advantage for applications of graphene and related 2D materials is that they can be produced on large scales by liquid phase exfoliation. The exfoliation process shall be considered as a particular fragmentation process, where the 2D character of the exfoliated objects will influence significantly fragmentation dynamics as compared to standard materials. Here, we used automatized image processing of Atomic Force Microscopy (AFM) data to measure, one by one, the exact shape and size of thousands of nanosheets obtained by exfoliation of an important 2D-material, boron nitride, and used different statistical functions to model the asymmetric distribution of nanosheet sizes typically obtained. Being the resolution of AFM much larger than the average sheet size, analysis could be performed directly at the nanoscale and at the single sheet level. We find that the size distribution of the sheets at a given time follows a log-normal distribution, indicating that the exfoliation process has a "typical" scale length that changes with time and that exfoliation proceeds through the formation of a distribution of random cracks that follow Poisson statistics. The validity of this model implies that the size distribution does not depend on the different preparation methods used, but is a common feature in the exfoliation of this material and thus probably for other 2D materials.

Received 31st December 2013
Accepted 28th February 2014

DOI: 10.1039/c3nr06919b

www.rsc.org/nanoscale

The huge scientific and technological interest for graphene has triggered in the last few years the development of a wide range of techniques to produce and process nanosheets that, having nanometric thickness and mesoscopic lateral size, shall be considered as *quasi* 2-dimensional (2D) objects. Besides their novel properties, even the way these 2D sheets are produced in solution, by exfoliation,[1] is an original process, still not completely understood.

The exfoliation of a 2D object from a 3D bulk material is a process spanning from the nano- to meso-scale due to bubble cavitation, intercalation and disruptive fragmentation, as we described in recent work.[2] Exfoliation always yields a polydispersed range of nanosheet thickness and lateral size. When characterizing these 2D sheet solutions, their average size and size standard deviation are commonly reported, often assuming that their size follows a "Gaussian" (a.k.a. "normal") distribution. Conversely, the experimental data show that the size distribution of these materials is highly asymmetric and non-Gaussian.

It is noteworthy that this asymmetry in size distribution shall be observed in very different systems such as the distribution of chemical elements in rocks, the species abundance in biology, the lengths of latent periods of infectious diseases in medicine, and the distribution of galaxies in astronomy (Fig. 1).[3,4]

A better modelling of the size distribution of 2D materials is needed both from a fundamental point of view (to understand the exfoliation mechanism) and from a technological point of view (to improve the metrology of 2D materials for applications and quality control).

Here, we used image processing of Atomic Force Microscopy (AFM) images to study the exfoliation and fragmentation process of a well-known 2D material, boron nitride (BN, Fig. 2), exfoliated in solution with two technologically relevant techniques: ultrasonication and ball milling. Exfoliated BN nanosheets are deposited on silicon and their size distribution and

[a]*Istituto per la Sintesi Organica e la Fotoreattività-Consiglio Nazionale delle Ricerche (ISOF-CNR), via Gobetti 101, 40129 Bologna, Italy. E-mail: palermo@isof.cnr.it*

[b]*Laboratorio MIST.E-R Bologna, via Gobetti 101, 40129 Bologna, Italy*

[c]*Istituto per la Microelettronica e Microsistemi-Consiglio Nazionale delle Ricerche (IMM-CNR), via Gobetti 101, 40129 Bologna, Italy*

[d]*Dipartimento di Ingegneria Civile, Ambientale e Meccanica, Università di Trento, via Mesiano, 77 I-38123 Trento, Italy*

[e]*Department of Chemistry "Giacomo Ciamician" University of Bologna, via Selmi 2, 40126 Bologna, Italy*

[f]*Laboratory of Bio-inspired & Graphene Nanomechanics, Department of Civil, Environmental and Mechanical Engineering, University of Trento, via Mesiano 77, 38123 Trento, Italy*

[g]*Center for Materials and Microsystems, Fondazione Bruno Kessler, via Sommarive 18, 38123 Povo (Trento), Italy*

[h]*School of Engineering & Materials Science, Queen Mary University of London, Mile End Road, London, E1 4NS, UK*

† Electronic supplementary information (ESI) available: Exfoliation methods, image analysis procedure, and comparison of sheet size on surfaces and in solution. See DOI: 10.1039/c3nr06919b

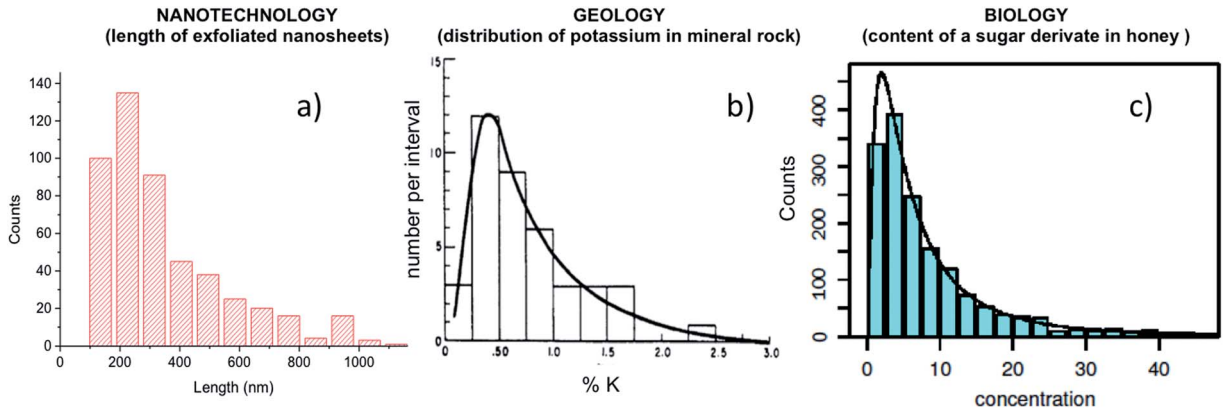

Fig. 1 Comparison of the typical size distribution obtained by exfoliation with other distributions observed in 2D materials, geology and biology. (a) Histogram of the length distribution of BN nanosheets obtained by liquid phase exfoliation. (b) Distribution of potassium in mineral rocks.[4] (c) Content of hydroxymethylfurfurol in honey.[3]

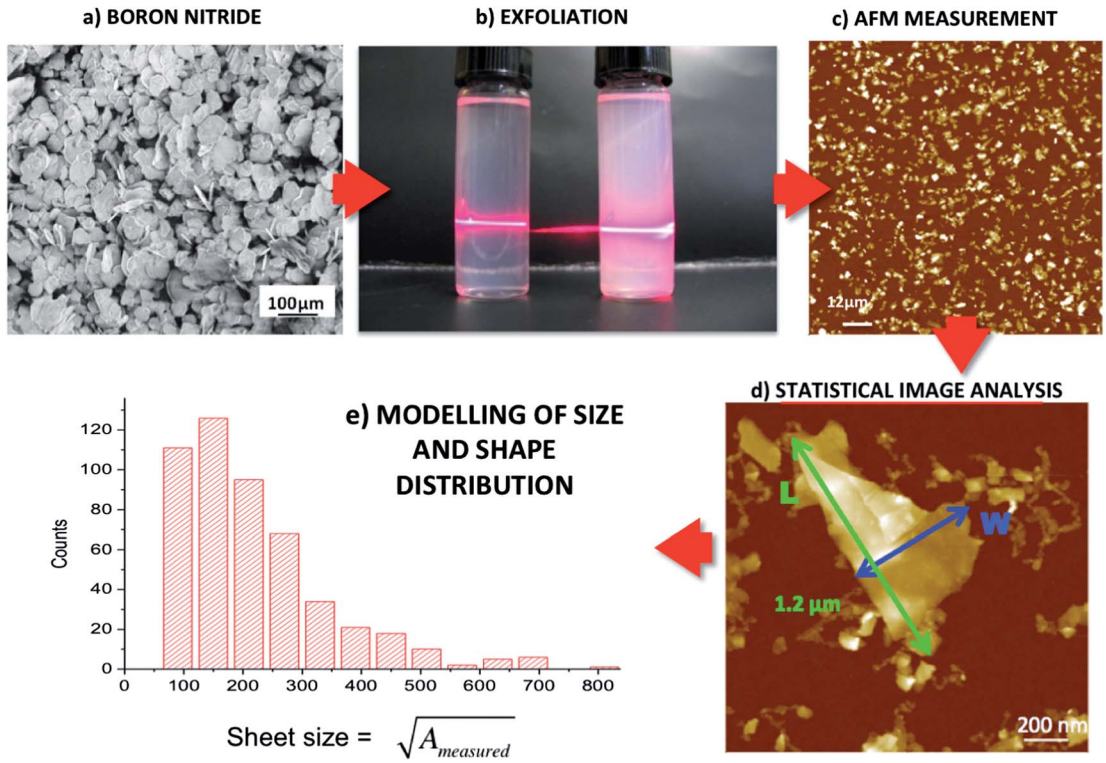

Fig. 2 (a) SEM image of the pristine BN flakes used for exfoliation. (b) Exfoliated solutions of BN in isopropanol, showing strong scattering due to the dispersed flakes. (c) AFM image of BN nanosheets spin coated on silicon oxide substrates. (d) Zoom-in of a single nanosheet, showing the typical way to define and thus estimate its length and width. (e) Histogram distribution of the sheet size obtained measuring the area of each sheet.

shape is measured by AFM and image analysis software, performing in this way statistics on *all* the sheets present on the surfaces, for a total of >6000 sheets, as compared to the tens of sheets analysed by manual Transmission Electron Microscope (TEM) statistics typically used for this task.[5] Being the resolution of AFM much larger than the average sheet size, the exact shape of each sheet shall be included in the statistics, allowing to cross-relate the length, the area and the length/width ratio of each sheet in each sample.[6]

By using a large statistical population we are confident to discriminate the most suitable analytic function able to reproduce the achieved fragment size distribution. As an example, by studying the galaxy distribution Brown *et al.* demonstrated that the universe underwent a single fragmentation event, separating into protogalactic volumes at a relatively early stage after the Big Bang.[7]

As a test material, we chose not to use the well-known graphene but used boron nitride, a relatively less studied 2D

material which has anyhow huge scientific and industrial interest, because it can be used as a monoatomic insulating layer for graphene-based electronic devices,[8,9] or as a bulk additive in polymers.[10]

Fig. 2 shows Scanning Electron Microscopy (SEM) images of typical BN flakes, and solutions obtained from such flakes by sonication or ball milling in isopropyl alcohol (IPA). The solutions obtained are stable for more than 6 months. BN solutions show a whitish colour and a strong light scattering (Fig. 2b), due to the presence of the BN nanosheets. Details of the different exfoliation procedures used are reported in the ESI (SI†). After exfoliation, the nanosheets were spin coated on silicon and measured by AFM (Fig. 2c and d).

To quantify the sheet size obtained with different techniques, we used image analysis software able to detect automatically individual sheets and measure their area and lateral size (Fig. 2e).[11] While AFM can easily give high-resolution images of the flakes and allow manual measurements of their size, several steps (image flattening, threshold selection, *etc.*) and careful analysis are required to obtain quantitative results, as detailed in the ESI.†

By using this approach, we could detect and digitalize hundreds of flakes having thickness down to 1 nm, deposited on areas of 1–400 μm^2.

Definition of sheet sizes and thus shapes

A particular issue in characterizing 2D nanosheets is to define the size of the sheets, because they have highly irregular shapes; we shall define for each sheet a given length L, measured along the longer segment and the maximal width W measured perpendicular to it (Fig. 2d).

For perfectly rectangular sheets the area A would be simply LW. This is not true for irregular shapes such as the ones typically obtained by exfoliation of 2D materials. However, image analysis software allows to measure pixel by pixel the area of each sheet, and use this as the relevant parameter to monitor exfoliation.

To have a reliable parameter, not depending on a particular shape, we thus used as a relevant size of the sheets the square root of the sheet area, measured pixel by pixel: $s = \sqrt{\mathrm{Area}_{\mathrm{meas}}}$. In the case of perfectly rectangular shapes, this would be simply $s = \sqrt{LW}$; for irregular sheets, this has the same dimensionality but is a more reliable parameter than length L. Different from L, s does not depend on the sheet shape, but only on the exact area.

Modelling of fragmentation processes

Fig. 3 shows that the statistical distributions of sheet sizes obtained with either sonication or ball milling do not follow a Gaussian distribution, but are strongly asymmetric and positively skewed, with a tail due to the presence of larger sheets in all samples. All the physical dimensions of the exfoliated sheets (length, width, area, and thickness) show the same asymmetric and non-Gaussian distribution (some examples are shown in Fig. S1 in the ESI†).

In general, skewed functions are the most general to describe the asymmetric distribution of a physical observable (*e.g.*, the size particle in powders or polymer blends). As an example, one of the most used distributions is the Poisson one, a discrete distribution that estimates the probability of a given number of events occurring in a fixed interval of space (distance, area or volume) and/or time if these events occur with a known average rate and independently from each other.[12] Poisson distribution is asymmetric and represents a very general case containing the well known and commonly used Gaussian distribution which is obtained as a limit of the Poisson one in the case of the total number of events $N \to \infty$.

Gaussian is a continuous symmetric distribution with the domain defined at all $\Re$; in particular the position of the peak (mode) coincides with the mean value (μ) and the median and the peak width are directly correlated with the standard deviation (σ); for these reasons, the Gaussian function is widespread and is commonly used to model several kinds of real distributions.

Given a distribution $f(\mu,\sigma)$, where μ is the distribution average and σ is the distribution standard deviation, Gaussian is a good approximation for $\mu/\sigma \gg 1$. This condition is not satisfied for the measured length, width and size distribution of the BN sheets, as clearly shown in Fig. 1, 3 and S1.† Moreover, the studied observables cannot be negative and the Gaussian distributions cannot be used to reproduce the measured ones.

For exfoliated 2D nanosheets, the mean value will not correspond to the median or to the highest peak of the size distribution, and the standard deviation will not be proportional to the half width of the distribution peak.

On the mathematic side, the importance of the Gaussian function is due to its role in the central limit theorem, which loosely says that the *sum* of a large number of independent quantities tends to have a Gaussian form, independent of the probability distribution of the individual measurements. This is the case, as an example, of the distribution of the x, y, z coordinates of particles diffusing in a solvent, coming from the sum of random scattering events.

When, instead, the final size is the result of the *product* of many independent, identically distributed actions, the final result is a highly skewed log-normal distribution. The skewed shape obtained in all exfoliation processes can thus be explained as the result of a more general fragmentation process,[3] where the size s of a sheet changes at each "cutting" event i as $s_i = s_{i-1}/c$.

In order to find the most appropriate analytic function to model exfoliation, we compared three continuous probability distributions commonly used to study the fragmentation processes: (LN) log-normal, (W) Weibull and (G) Gamma function. A comparison of the properties of these functions is reported in Table S1 in the ESI.†

LN represents the distribution of a random variable whose logarithm is normally distributed. If the random variable x is log-normally distributed, then $X = \log(x)$ has a Gaussian distribution. LN is characteristic of a random multiplicative

process, and has previously been used to describe many rock crushing processes.

The Weibull function was the first function applied by Rosin & Rammler in 1933 to describe a particle size distribution.[13] The W function describes the size distribution given by a series of fragmentation events which are not constant and whose rate is proportional to a power of size: $\tau = s^k$, where k is the exponent of the power law.

The Gamma function is the generalization of the Maxwell–Boltzmann distribution and it is used to study the collisional fragmentation problem.[14] Moreover, G distribution functions are known to provide a very good fit to the distribution of cell sizes in Voronoi textures (*i.e.* area in 2D partitioned Euclidean spaces).[15]

Fig. 3 shows the measured size distribution of sheet size $f(s)$, obtained by sonication and ball milling with high and low power (see SI† for details). To avoid any artefacts we used for the fit only sheets having $s > 50$ nm, significantly larger than the AFM resolution. Experimental data have been fitted using different statistical distributions: LN (black line), W (blue line) and G (green line). In general, it is difficult to discriminate between the log-normal, Weibull and even Gamma distributions in particle size distribution curves as evident from the figure; the coefficient of determination (R^2) is 0.93–0.94 for all the three curves (the closer is the R^2 value to 1, the better is the fitting).

In order to overcome this well-known problem (see ref. 16 for example), we studied the complementary cumulative distribution functions: $N(s) = N(s_{TOT}) - \int_0^s f(x)\mathrm{d}x$, calculated by the best fits of three curves. Given a size s, the $N(s)$ function indicates the number of sheets *larger* than s, for this reason it is also called the *survival* or *reliability* function.

The measured distribution and the calculated curves are displayed in Fig. 4 using a semi-log scale visualization. The comparison between all the curves shows clearly that the experimental distribution $N(s)$ of sheet sizes follows a log-normal curve. The sheet distribution obtained with very different methods (sonication and ball milling) can thus be fitted using the same model, suggesting that the sheet size distribution does not depend on the details of the preparation methods, but is instead a common feature in the exfoliation of 2D materials. This kind of "universal behaviour" is not surprising, and has been observed in different disciplines.[3] The presence of log-normal behaviour is characteristic of a random multiplicative process; it indicates that exfoliation follows a linear fragmentation model, *i.e.* a process where the fragmentation is only driven by an external source (in this case, ultrasounds or milling balls) and where the repeated collisions between fragments can be neglected. [17]According to the Kolmogorov theory,[18] the LN distribution represents the final size distribution in the limit of small BN fragments originated from a "mother cluster" which broke into

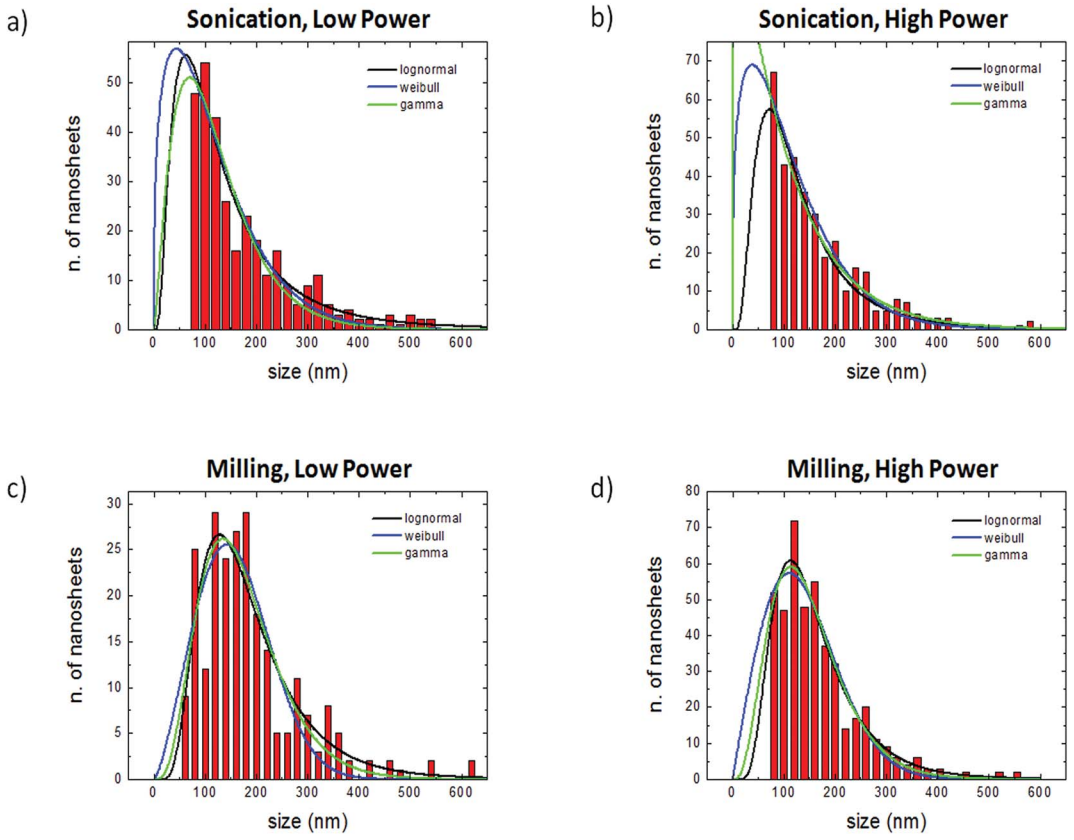

Fig. 3 Nanosheet size distribution obtained with sonication and ball milling, using different preparation conditions. A fit of the experimental data using log-normal, Weibull or Gamma distributions is also reported in black, blue, green lines respectively.

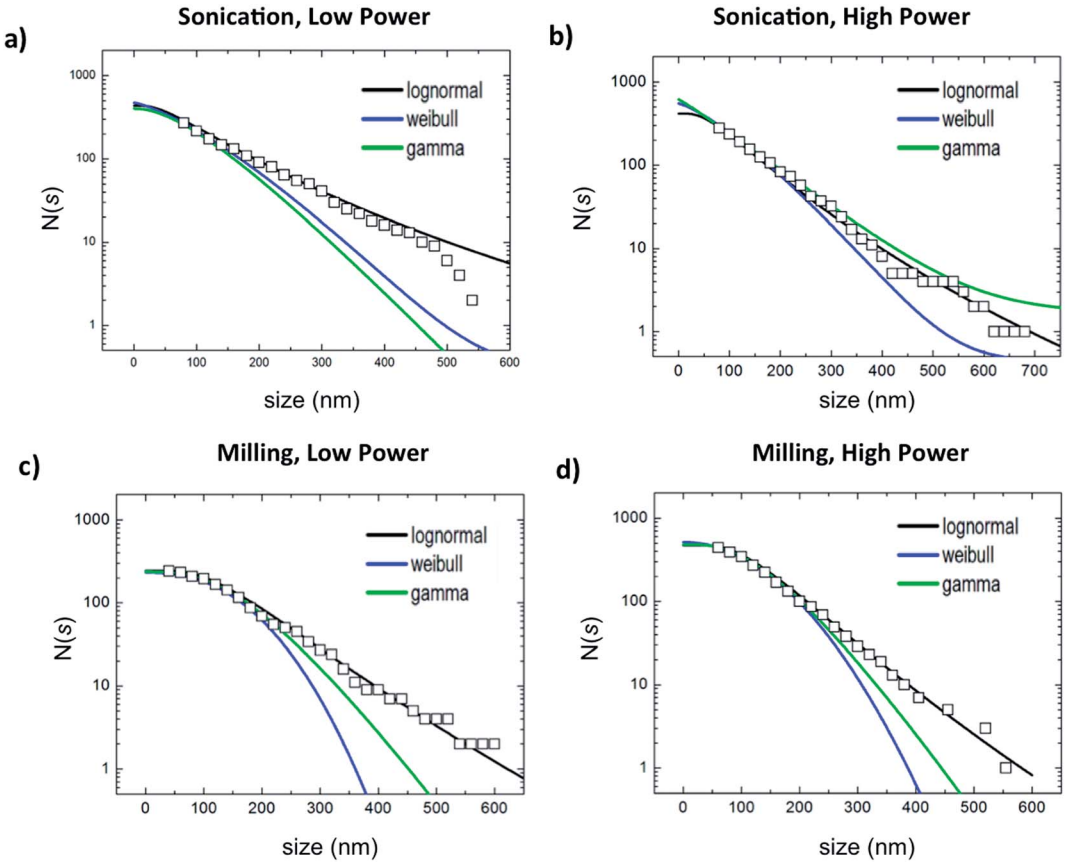

Fig. 4 Survival distribution functions (empty squares) corresponding to the data shown in Fig. 3. A fit of the experimental data using log-normal, Weibull or Gamma distributions is also reported in black, blue, green lines respectively.

random-sized fragments through a stochastically determined process (Markov process). The regime of limit of small fragments corresponds to the case in which the fragmentation is completely described by rupture-like breakup events while the erosion-like events (described by a size distribution with a bimodal shape) can be completely neglected.

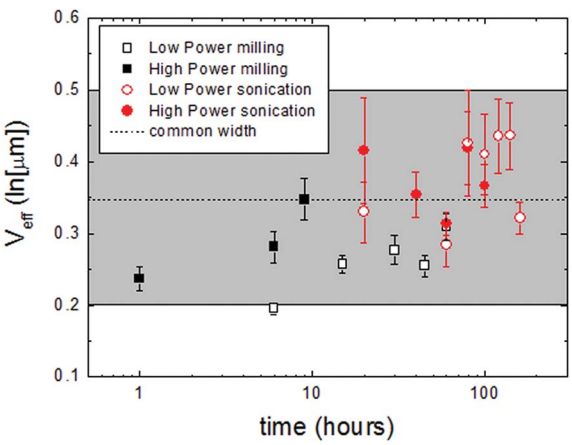

Fig. 5 Effective variance of the log-normal distribution observed for all samples. The shaded area indicates the 0.2–0.5 "universal" variance observed in several different cases in the literature.[19]

Not only many different variable distributions follow a log-normal behaviour, but even the width of these log-normal distributions (calculated as the variance of the normalized unit $S = \ln s/s_{mode}$) ranges from about 0.2 to 0.5 in several different cases in the literature.[19]

We calculated the effective distribution widths V_{Eff} for all our samples (Fig. 5); while, as could be expected, variance increases slightly with processing time, all values found to lay within the range 0.2–0.5 indicating that the fragmentation event is nearly binary, *i.e.*, one flake is divided into two flakes, with no "multiple fragmentation" events.[19] In simpler words, in the assumed fragmentation $s_i = s_{i-1}/c$ we have $c \approx 2$.

Last but not least, it can be seen that the distribution decay is linear for large s, indicating that exfoliation proceeds through the formation of a distribution of random cracks that follow Poisson statistics.[7,20]

Shape analysis of the exfoliated sheets

Using image processing of the AFM images, we could also calculate the length/width aspect ratio for all the samples. We found that, even if the sheet's size spans over nearly two orders of magnitude (within the range between 30 and 1000 nm), the overall length/width (L/W) ratio is fairly constant, being $\approx$2.8 for sonication and $\approx$2.6 for milling (see Fig. 6a; all graphs

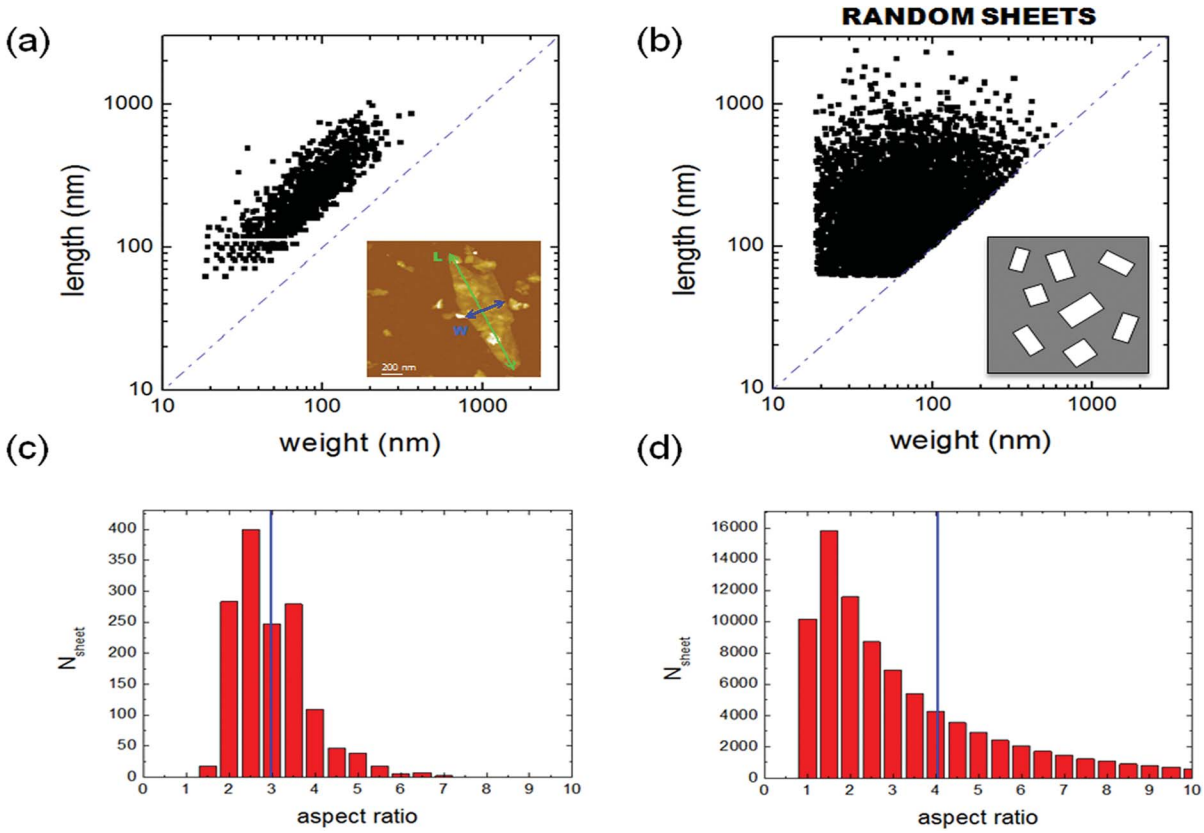

Fig. 6 Length/width plots of BN sheets (a) measured in the case of high power sonication and (b) calculated by random distributions, plotted in the log–log scale. Blue dash-dotted line represents the case of aspect ratio = 1. (c and d) Corresponding L/W ratio distributions (red bars) (c) measured in the case of high power sonication and (d) calculated by random distributions. Blue vertical lines show the mean values.

showing the data points analysed are shown in Fig. S2†). Summarizing, the (L/W) ratio only depends on the fragmentation technique, but does not show any appreciable variation in the processing time and/or processing conditions.

To check if this ratio is simply due to a random distribution of sheets' shape, we compared it with the L/W ratio of artificial, computer-generated rectangles having random sides a and b spanning the same size range observed for real nanosheets. Fig. 6 shows length *vs.* width plots obtained from experimental data (Fig. 6a) or from computer-generated rectangles with random, uncorrelated length and width (Fig. 6b).

The experimental data in Fig. 6a were obtained from the AFM analysis of more than 1400 sheets produced by sonication and ball milling at different times. The artificial data in Fig. 6b were instead obtained generating rectangles where the sides of each rectangle are uncorrelated, even if having a log-normal distribution with the same mean values and standard deviation as the experimental ones.

The calculated distribution in Fig. 6b clearly shows different behaviours with respect to the measured ones and has a L/W ratio $= 4.0 \pm 0.1$, significantly larger than that obtained from the measurements. The experimental length and width of sheets are thus correlated, as visible in Fig. 6a and S2,† and their ratio is not a random value. This suggests that the shear stress of 2D sheets along different directions yields fracture probability of sheets having a preferred L/W aspect ratio. This ratio is slightly larger for sonication ($L/W \approx 2.8$, likely due to the aligning effect of collapsing cavitation bubbles[21]) than in ball milling ($L/W \approx 2.6$) where the shear force can cleave the BN flakes from their outer surfaces, while the compression force can crush and delaminate thin nanoplatelets acting on their edge.[22] SEM images of BN mesoscopic flakes cleaved by different shear forces are shown in Fig. 7. The effects of shear and compression action of the milling spheres are visible on several flakes, with BN stacks shifted over each other, showing folds not only on the surface of the platelets, due to the shear force of balls impacting on the top surface of the particle, but also *inside* the platelets due to the compression force of milling balls colliding with the edge of the particles.[23]

Sheet size evolution with time

We studied the evolution of average size at increasing processing times, that we call $s_{mean}(t)$. As mentioned above, we should keep in mind that this average value will not correspond to the median or to the highest peak of the size distribution $N(s)$, because it is not Gaussian.

The AFM size analysis, performed on surfaces at the nanoscale, gives similar results to macroscopic DLS measurements performed in solution, but with an offset (DLS gives an estimated size that is larger than the AFM measured one of *ca.* 20%, see ESI† for more details).

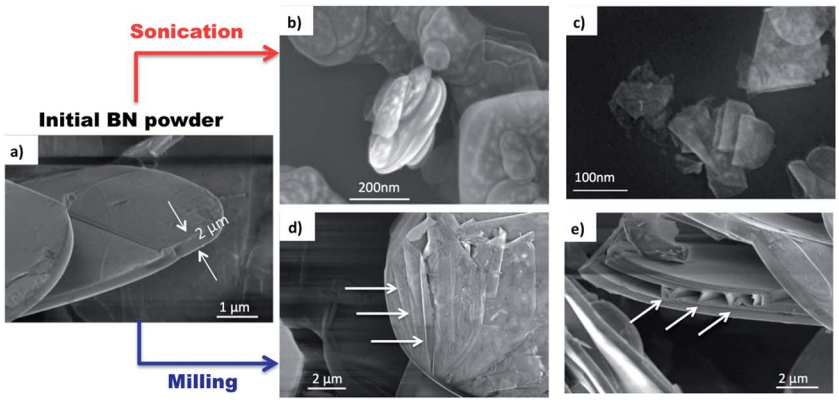

Fig. 7 SEM images of the BN platelets before (a) and after treatment by sonication (b, c) and milling (d, e). Flakes with BN stacks shifted over each other, showing folds not only on the surface of the platelets (white arrows) due to the shear force of balls impacting on the top surface of the particle (d), but also inside the platelets, (white arrows) due to the compression force of milling balls colliding with the edge of the particle and then sliding over it (e).

LN distribution is observed for all the used fragmentation procedures and for different times. Hansen *et al.*[24] observed that the size scales with time as an inverse power-law: $s_{\mathrm{mean}} \propto t^{-1/\lambda}$ (Fig. S3†), where λ (a.k.a. homogeneity index) is the exponent of the overall rate of breakup $a(s) \propto s^{\lambda}$. According to this model, higher values of λ indicate that the fragmentation speed is strongly dependent on the sheet size.

In our sonication experiments, the value of λ (homogeneity index) goes from 8 ± 1 to 4.5 ± 0.6 with increasing sonication power, suggesting that in high power sonication, with high shear rates, the probability of breaking is more uniform for sheets of different sizes.

A similar inverse power-law dependence (with $\lambda = 2$) has been recently reported by Khan *et al.*[25] exploiting a theory previously involved to reproduce the length distributions of sonication of 1D nanotubes[21] to model the size reduction of sonicated graphene sheets.

We note that the application of models developed for 1D objects to 2D shapes is not straightforward. A 1D nanotube can be defined with a single dimension L and can be broken in just one direction, perpendicular to its long axis; conversely, a 2D sheet can be broken in different directions, shall have different length/width ratios, and thus have a different evolution of the average area or average lateral size with processing time. Moreover, the power law should depend on the power dissipated during the fragmentation events.

Finally, the statistical procedure described here was used to compare the average size of BN sheets obtained by high sonication and milling. The asymptotic values are 105 ± 7 nm and 100 ± 8 nm, for high and low power sonication, while for milling we obtain 142 ± 8 nm and 136 ± 4 nm, respectively for high and low power. We underline that (different from size distributions discussed above) these numbers are not universal results but depend on the exfoliation conditions used such as processing conditions, time, solvent, *etc.*

To test the processability of the obtained materials, we used them to produce BN paper membranes by filtering the solution on filter paper. Upon removal of the filter, we obtained uniform membranes of BN, robust enough to be handled and further processed (Fig. S5†).

In conclusion, we characterized the size distribution of BN nanosheets produced in solution by sonication and ball milling. In all the different samples tested, the cumulative size distribution of the sheets at a given time follows a log-normal distribution.

We did not observe a power-law distribution of sizes that would imply a scale-invariant exfoliation process. The failure of the power-law curve indicates that the exfoliation process does not follow the fractal law, but rather has a "typical" sheet scale length.

The log-normal best-fit curves obtained show a very good linearity in a semi-log scale (black lines in Fig. 4) within the data range ($R^2 = 0.9936$). This behaviour corresponds to the simplest case of the empirical Rosin–Rammler equation,[26] indicating that for both sonication and ball-milling techniques, exfoliation proceeds through the formation of a distribution of random cracks that follow Poisson statistics.[7,20] The fragmentation can be simply described as the process mainly driven by an external source and completely described by rupture-like breakup events.

Acknowledgements

The research leading to these results has received funding from the European Union Seventh Framework Programme under grant agreement no. 604391 Graphene Flagship, the EC Marie-Curie ITN-GENIUS (PITN-GA-2010-264694), the FET project UPGRADE (project no. 309056), the Operative Program FESR 2007-2013 of Regione Emilia-Romagna – Attività I.1.1 and the European Research Council (ERC grants: Bihsnam, Replica[2] and Knotough).

References

1 J. N. Coleman, M. Lotya, A. O'Neill, S. D. Bergin, P. J. King, U. Khan, K. Young, A. Gaucher, S. De, R. J. Smith,

I. V. Shvets, S. K. Arora, G. Stanton, H. Y. Kim, K. Lee, G. T. Kim, G. S. Duesberg, T. Hallam, J. J. Boland, J. J. Wang, J. F. Donegan, J. C. Grunlan, G. Moriarty, A. Shmeliov, R. J. Nicholls, J. M. Perkins, E. M. Grieveson, K. Theuwissen, D. W. McComb, P. D. Nellist and V. Nicolosi, *Science*, 2011, **331**, 568–571.

2 Z. Y. Xia, S. Pezzini, E. Treossi, G. Giambastiani, F. Corticelli, V. Morandi, A. Zanelli, V. Bellani and V. Palermo, *Adv. Funct. Mater.*, 2013, **23**, 4684–4693.

3 E. Limpert, W. A. Stahel and M. Abbt, *Bioscience*, 2001, **51**, 341–352.

4 L. H. Ahrens, *Geochlmlca et Coemoehlmlca Acta*, 1957, **5**, 49–73.

5 Y. Hernandez, V. Nicolosi, M. Lotya, F. M. Blighe, Z. Y. Sun, S. De, I. T. McGovern, B. Holland, M. Byrne, Y. K. Gun'ko, J. J. Boland, P. Niraj, G. Duesberg, S. Krishnamurthy, R. Goodhue, J. Hutchison, V. Scardaci, A. C. Ferrari and J. N. Coleman, *Nat. Nanotechnol.*, 2008, **3**, 563–568.

6 J. Russier, E. Treossi, A. Scarsi, F. Perrozzi, H. Dumortier, L. Ottaviano, M. Meneghetti, V. Palermo and A. Bianco, *Nanoscale*, 2013, **5**, 11234–11247.

7 W. K. Brown, R. R. Karpp and D. E. Grady, *Astrophys. Space Sci.*, 1983, **94**, 401–412.

8 L. Britnell, R. V. Gorbachev, R. Jalil, B. D. Belle, F. Schedin, A. Mishchenko, T. Georgiou, M. I. Katsnelson, L. Eaves, S. V. Morozov, N. M. R. Peres, J. Leist, A. K. Geim, K. S. Novoselov and L. A. Ponomarenko, *Science*, 2012, **335**, 947–950.

9 B. Hunt, J. D. Sanchez-Yamagishi, A. F. Young, M. Yankowitz, B. J. LeRoy, K. Watanabe, T. Taniguchi, P. Moon, M. Koshino, P. Jarillo-Herrero and R. C. Ashoori, *Science*, 2013, **340**, 1427–1430.

10 U. Khan, P. May, A. O'Neill, A. P. Bell, E. Boussac, A. Martin, J. Semple and J. N. Coleman, *Nanoscale*, 2013, **5**, 581–587.

11 Editon edn, Scanning Probe Image Processor, version 2.0000, Image Metrology A/S, Lyngby, Denmark.

12 J. Frederick, *Statistical Methods In Experimental Physics*, World Scientific Publishing Co Pte Ltd, Singapore, 2nd edn, 2006.

13 P. Rosin and E. Rammler, *Inst. Fuel*, 1933, **7**, 29–36.

14 M. Kostoglou and A. J. Karabelas, *J. Colloid Interface Sci.*, 2006, **303**, 419–429.

15 M. A. Fortes and P. N. Andrade, *J. Appl. Phys.*, 1988, **64**, 5157–5160.

16 G. M. Kondolf and A. Adhikari, *J. Sediment. Res.*, 2000, **70**, 456–460.

17 Z. Cheng and S. Redner, *Phys. Rev. Lett.*, 1988, **60**, 2450–2453.

18 N. A. Kolmogorov, *Transl. in English by Levin in NASA-TT F-12,287 (1969)*, 1941, **31**.

19 K. Hosoda, T. Matsuura, H. Suzuki and T. Yomo, *Phys. Rev. E.*, 2011, **83**(3), 031118.

20 D. L. Turcotte, *J. Geophys. Res., [Solid Earth Planets]*, 1986, **91**, 1921–1926.

21 F. Hennrich, R. Krupke, K. Arnold, J. A. R. Stutz, S. Lebedkin, T. Koch, T. Schimmel and M. M. Kappes, *J. Phys. Chem. B*, 2007, **111**, 1932–1937.

22 Y. G. Yao, Z. Y. Lin, Z. Li, X. J. Song, K. S. Moon and C. P. Wong, *J. Mater. Chem.*, 2012, **22**, 13494–13499.

23 L. H. Li, Y. Chen, G. Behan, H. Z. Zhang, M. Petravic and A. M. Glushenkov, *J. Mater. Chem.*, 2011, **21**, 11862–11866.

24 S. Hansen, D. V. Khakhar and J. M. Ottino, *Chem. Eng. Sci.*, 1998, **53**, 1803–1817.

25 U. Khan, H. Porwal, A. O'Neill, K. Nawaz, P. May and J. N. Coleman, *Langmuir*, 2011, **27**, 9077–9082.

26 J. J. Gilvarry, *J. Appl. Phys.*, 1961, **32**, 391.

SUPPORTING INFORMATION

Exfoliation methods

Two different techniques (sonication and ball milling) were used to prepare the samples, with two different conditions each (high and low power, see table S2). Fig. 2 in main text shows SEM images of the starting BN powder and of the typical solutions obtained.

For sonication test, suspensions were prepared at same starting concentration (3 mg/ml) in IPA and sonicated at different times (20, 40, 60 and 80 hours) using an Elmasonic P70 Ultrasonic Bath at 220W or 66W of effective power.

A planetary ball mill (Retsch PM100) with a 50 ml Zirconium dioxide grinding jar and ≈1300 zirconium oxide balls (3 mm in diameter) was used to mill BN powders in IPA at different times (from 1 to 60 hours) and rotation speeds (200 and 450 rpm). After the exfoliation, a centrifuge Heraeus (Omnifuge 2 RS) was used to remove the larger, mesoscopic BN particles.

Upon exfoliation, BN solutions show a whitish colour and a strong light scattering (Fig. 2c), due to the presence of the BN sheets. At difference with graphene, that is exfoliated using high boiling solvents, we exfoliated BN using as solvent isopropanol (IPA) which is a low boiling point solvent (b.p.=82 ºC), quick to volatilize and easy to remove after BN processing on surfaces or in composites, thus minimizing processes of flake aggregation. Exfoliation in IPA yields stable solutions of BN.

Both in ball milling and sonication mechanical forces act on the material; however, these forces have a different origin and work on different scale lengths. In ball milling, the exfoliation is due to compression or shear forces caused by the movements of the balls, that in our case have a macroscopic diameter (3 mm). In sonication, the mechanical action arises from cavitation

bubbles, with radius of about one hundred of μm, that generate high strain rates in the surrounding liquid upon implosion. [1-3]

Fig. 7 in main text shows the typical effects of treatment by sonication (Fig. 7b,c) and milling (Fig. 7d,e) on BN.

Sonication reduces the size of mesoscopic flakes, but does not change significantly their morphology. We previously studied the effect of sonication on materials by monitoring the evolution of surface roughness on bulk graphite sonicated in a solvent commonly used for graphene production, *N*,*N*'-dimethylformamide;[3] in these conditions exfoliation proceeds on a layer-by-layer basis; only the upper part of the graphite is interested, and the process is slow, requiring several hours to have visible effects on the substrate roughness.

In case of milling, instead, the effects of shear and compression action of the milling spheres is visible on several flakes, with BN stacks shifted over each other, showing folds not only on the surface of the platelets (Fig. 7d, white arrows) due to the shear force of balls rolling over the top surface of the particle, but also *inside* the platelets, (Fig. 7e, white arrows) due to the compression force of milling balls colliding with the edge of the particle and then sliding over it, in agreement with the results obtained in ref. [4].

Both milling and sonication yield a large number of BN sheets after spin coating on silicon oxide substrates. The amount of exfoliated material estimated by AFM is found to be roughly proportional to BN concentration in solution. By assuming for BN an extinction coefficient α=2367 ml/mg/m measured at 300 nm, [5] an estimated concentrations up to 0.04 mg/ml, comparable to 0.06 mg/ml obtained by extensive sonication could be estimated; however, the presence of significant light scattering due to the large size of the sheets does not allow to use optical absorption data to estimate exfoliation yield. The absorbance *A* of all solutions showed a

power-law dependence of A on light wavelength λ ($A \propto \lambda^{-n}$), indicative of strong light scattering, in agreement with what observed in ref. [5].

The sheet morphology, as measured by AFM, is the one expected for layered materials, with linear edges and sharp corners (Fig. 2d), but the sheets have a wide distribution in lateral size (from tens of nm to more than 1 μm) and thickness (up to 10 nm, with no large macroscopic aggregates). It is thus difficult to discriminate any difference just by visual comparison of the AFM images.

Image analysis procedure

To characterize and define effectively nano-materials is a major metrological problem; as example, the exfoliation of the same starting solution shall give different yields of solubilized material and monolayers fraction if centrifuged at different speeds,[6] or purified using different washing procedures.[7,8]

It is fundamental to quantify not only the average size of the sheets obtained, but their size distribution as well; in this, 2D materials have some analogy with what is done routinely to characterize poly-dispersed, 1D polymers.[9]

For this, statistical analysis is needed to characterize the poly-dispersed sheets. This is commonly done through one-by-one localization and analysis of exfoliated sheets with Transmission Electron Microscopy (TEM). This approach, besides bring tedious and cumbersome, is also not fully objective, because smaller sheets shall escape from the TEM grid thus over-estimating the mean sizes of the exfoliated flakes and making the related statistics inaccurate. For example, the measurement uncertainty depends on the square root of the number of the detected sheets in case

of ensembles following Poisson statistics. Thus, a sample population of 100 measured sheets is associated with 10% of intrinsic error. The operator as well shall sometime focus on examining the most interesting (i.e. thinner) sheets while missing larger aggregates. Furthermore, sheets aggregation, restacking and folding on the TEM grid during solvent evaporation makes the analysis of size and shape of the sheets difficult. The number of sheets localized and measured by TEM can be very low, even below ten for a given nanosheet type, and even partially folded or overlapping sheets should be measured to improve the statistics. [10]

Thus, it is fundamental to complement published results obtained by TEM with more detailed studies, performed at the nanoscale and on large statistical data (see also section dedicated to Dynamic Light Scattering in the following text).

Atomic Force Microscopy (AFM) can be used to characterize the size distribution of thousands of nano-sheets, to automatically detect and analyze the length, area and surface density of them, and to compare the obtained results with more macroscopic characterization techniques such as optical spectroscopy and dynamic light scattering.

To quantify the sheet size obtained with different techniques, we used an image analysis software able to detect automatically individual sheets and measure their area and lateral size[11]. In this way we could also remove noise and grains crossing the image edge, and plot the statistical distribution of the different observables measured. While AFM can easily give high-resolution images of the flakes and allow manual measurements of their size, several steps are required to obtain quantitative results on a statistical base.

a) Use of a flat substrate allowing a fast and unambiguous discrimination of the flakes from the surrounding bare substrate. This primary condition was satisfied by spin coating BN on atomic flat silicon substrate because the height of the single sheet (about 1 nm thick as measured by

AFM) is significantly larger than the root mean square roughness (RMS) of the substrate which amounts to 1.8 Å.[12]

b) Use of the correct flattening procedure to remove the AFM artefacts due to sample tilt, always present, and non-linearity of the piezoelectric scanner. [13,14] Dedicated flattening procedures based on local mean or local standard deviation (SD) of the height values shall be used in case of irregular surfaces.[11] The first method simply subtracts the mean value of the pixels in the local neighbourhood of each pixel. The SD equalization scales the height values by a factor given by the standard deviation of the global image, divided by the local mean of the standard deviation. The efficiency and the reliability of the flattening procedure were monitored step-by-step by histogram analysis, plotting the frequency distribution in z of all the pixels of each image. In case of relatively flat substrates, the better is the flattening, the narrower is the measured height histogram, with a peak-width close to silicon roughness. The used procedure removes the artifacts in few steps and the measured substrate roughness rapidly converges in the range of values between 0.15 and 0.20 nm, in good agreement with the values reported in literature.

c) Once the image is flattened, a suitable height threshold is used to discriminate flakes from background. A binary condition selection is used: only the pixels above the threshold are considered belonging to a flake, while the rest is disregarded. Anything having a height lower than the threshold will be counted as background, and not included in the statistics. We choose 0.5 nm as a suitable threshold, a value half the thickness of a typical sheet and more than two times larger than the substrate RMS roughness.

d) A further filter shall also be applied. The filter will simply exchange small "ridge pixels" with interpolated values if the slope on the ridge is smaller than the given percentage of the maximum slope. We define a ridge pixel as a pixel having a value that is either larger or smaller than its

four next-neighbour pixels. In contrast to other filters, this filter will only affect the smaller corrugations. To eliminate larger noise peaks a Local Mean filter could be applied (see above).

e) Recognise connected or partially overlapping flakes by finding local minima, even above the threshold, that will be considered as flake edges.

Even if the software performs automatically all these operations, the parameters used for each operation (threshold height, noise filter, etc.) should be carefully tuned and cross-checked for reproducibility and reliability. However, the automatic detection of flakes is pretty robust and not so sensible to fine-tuning of these parameters, given that the flakes are usually deposited on very flat silicon substrates and that the lateral resolution of AFM is much larger than the average sheet size. In particular, we have found that the method is very suitable to analyze structures having a lateral size of tens of nanometers and uniform thickness, such as flakes of graphene, BN or other 2D materials. More details on the flake detection procedure shall be found in ref. [11].

The first output of the AFM statistical analysis is simply the amount of sheets obtained for each process and treatment time, expressed in terms of number of sheets per square micron plotted in Fig. S6. Insets in Fig. S6 show the typical AFM images obtained at initial and final stages of the exfoliation, where the image analysis software has automatically identified and assigned a different colour to each BN sheet.

Of course, the most interesting output of the analysis is not the simple number of sheets, but their lengths and area (or size) distribution that was already discussed in main text.

We tried to use statistical histogram analysis to measure as well the AFM thickness of the sheets, as previously done with organic self-assembled monolayers [15] and with mono-atomic graphene oxide sheets. [16] However, the height histograms obtained did not yield well-defined peaks corresponding to the different BN layers, due to the strong dependence of this measurement on

the roughness of the sheets, which often show the presence of partial folds and nano-debris. Thus, the thickness was measured manually by profile analysis of different AFM scans, showing a skewed distribution similar to the ones observed for length (fig. S1). The thickness shows as well a decreasing trend (Fig. S7) similar to what observed for lateral size, with most of the material present as multi-layered sheets, and with all the samples distribution approaching an asymptotic average thickness of ≈ 6 nm; the values of average final thicknesses measured by AFM were: 8±4 nm (High P. sonication), 6±3 nm (Low P. sonication), 6±3 nm (high P. Milling), 6±3 nm (low P. milling). As mentioned in main text, we should keep in mind that these average values will not correspond to the median or to the highest peak of the size distribution *N(s)*, because they are not Gaussian.

Comparison of sheet size on surfaces and in solution

Statistically efficient techniques, able to estimate particle size quantitatively on large scale and in solution are light scattering techniques, [17] such as dynamic light scattering (DLS) that has already been used to quantify the size and shape of graphene or graphene oxide (GO) sheets in solutions.[18,19] A recent work has demonstrated that there is an empirical relationship between the sheet size measured by TEM and by DLS that, even if having relative errors up to 40%, shall be used to give a quick estimate of the average size of solubilized sheets.[10] DLS measurements are affected by two key properties: solvation and sample shape. While the first kind of overestimation can be simply neglected for mesoscopic objects, the second point is not trivial. The DLS measurement is based on the assumption that all particles undergo Brownian motion in the solution and diffuse in the liquid like spherical particles; instead, 2D anisotropic sheets have

different diffusion coefficients, and thus one could not assume *a priori* that DLS will give the right measurement. [18,19]

For a perfect sphere, Brownian motion is the same in all directions; for a linear nanostructure (like a nanotube), Brownian mobility is larger along the optical axis. For 2D sheets the large optical anisotropy shall align the flake orthogonal to the light polarization, with increased fluctuations in both longitudinal and transverse directions due to a higher contribution from rotational motion with respect to nanotubes, as demonstrated for graphene by Ferrari and co-workers.[20]

The size evolution observed by AFM was thus compared with measurements performed in solution by DLS. The correspondence between the two techniques shall never be straightforward: AFM measures the sheets one by one, with high resolution, on a solid surface whereas DLS measures thousands of sheets at once, while floating in solution.

Fig. S3 and Fig. S5 compare the BN sheet size as measured by AFM and DLS. We see that both AFM and DLS techniques give a similar trend in size evolution, but with an offset between the measured *s*. A recent work by Coleman and coworkers [10] reports for 2D materials an empirical power law correlation between the graphene nanosheets length, measured by TEM, and the first peak of the particle size distribution $a_{DLS} \propto L^{2/3}$. In our case, this empirical finding does not apply because we were interested in the original size distribution and did not perform any sorting of nanosheets size by centrifugation. Finding the right correlation between DLS signal and the "true" size of flexible, monoatomic, 2-Dimensional objects in solution will require much more experimental and theoretical work, and is out of the scopes of this paper. All we shall safely say is that, averaging on all samples, DLS gives an estimated size that is larger than the AFM measured one of ca. 20%. The 20% difference we observed between the size of a 2D sheet

measured on surface and in solution can be due to the complex hydrodynamic radius, the folding and the unknown refractive index of these 2D sheets in solution, that does not allow to use the Mie theory commonly used in DLS to infer the particles' radius from the scattering spectrum.

Final remarks: which is the best nanosheet shape for composites?

Overall, the statistical comparison of the samples indicates that the four different techniques give comparable results, with a lateral sheet size between 116 and 136 nm (as measured by AFM) and an average thickness of 6 nm, with a lateral size/thickness aspect ratio ≈20.
The relevant size that should be monitored depends on the final application of the material; in general, for composites applications, both length and width are relevant and should be optimized. In particular, in order to produce stronger composites, the load transfer must be maximized and this would correspond to have a length larger than a critical minimal value (along the applied load) of the flake $L_{min} \approx \sqrt{thE/G}$, where h is the thickness of the interface between matrix and the few layer graphene flake, t is its total thickness, E is the Young modulus of graphene and G is the shear modulus of the interface[21]. In order to have all the graphene mass working in the composite this minimal length is also the optimal one. However, because of the random orientation of the sheets, load transfer will take place along all sides of the sheets, and thus the size distribution of both L and W should be taken into account; maximizing both length and width means maximizing the average area of the sheet, to give a very good interaction with the surrounding matrix.

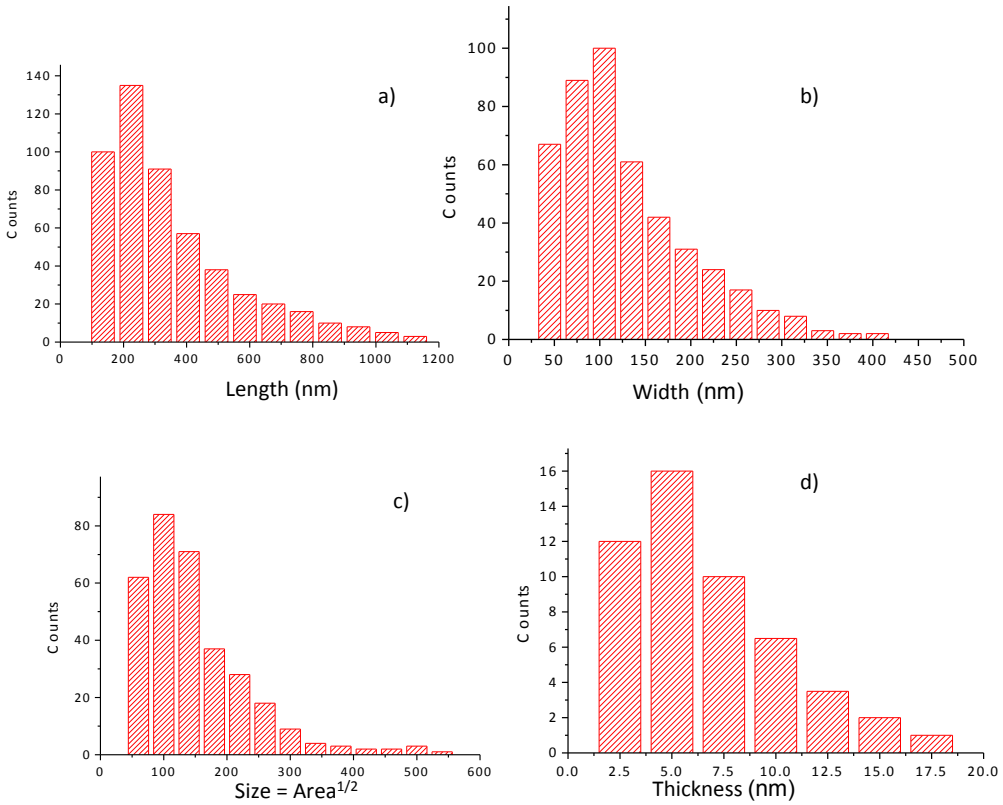

Fig. S1 Typical histogram distributions of various physical quantities of the nanosheets obtained by AFM image analysis, all featuring an highly skewed shape.

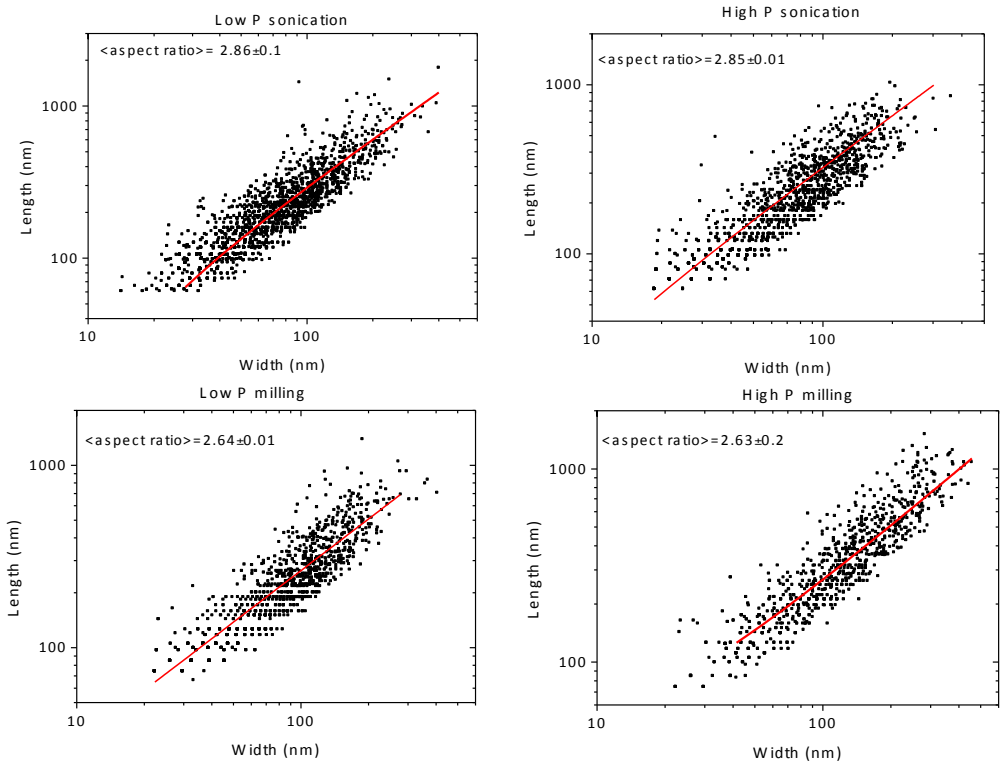

Fig.S2 Aspect ratio of length to width for all the BN samples exfoliated by milling and sonication, plotted in log-log scale. Red lines show the best linear fitting of the data points. The average slope is reported with its standard error in the inset of each graph.

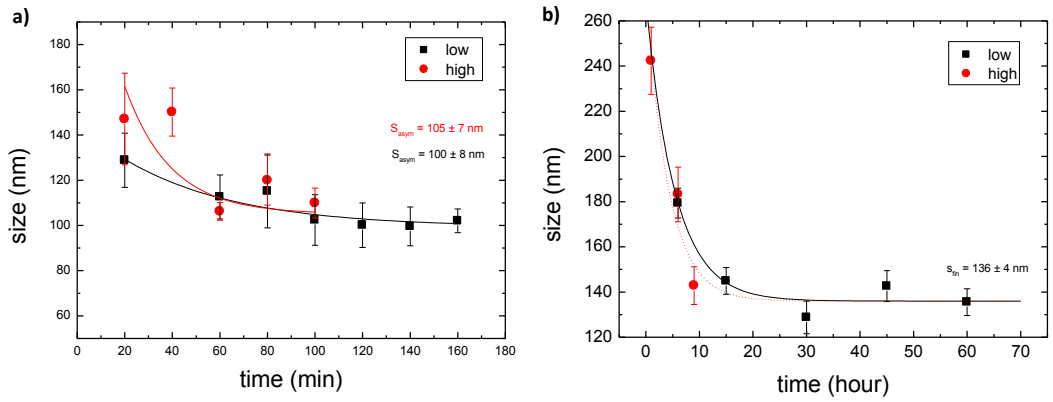

Fig. S3 Evolution of BN nanosheet size exfoliated by ultrasonication and Ball milling measured on a surface by AFM. All the data-set are fitted with exponential curves.

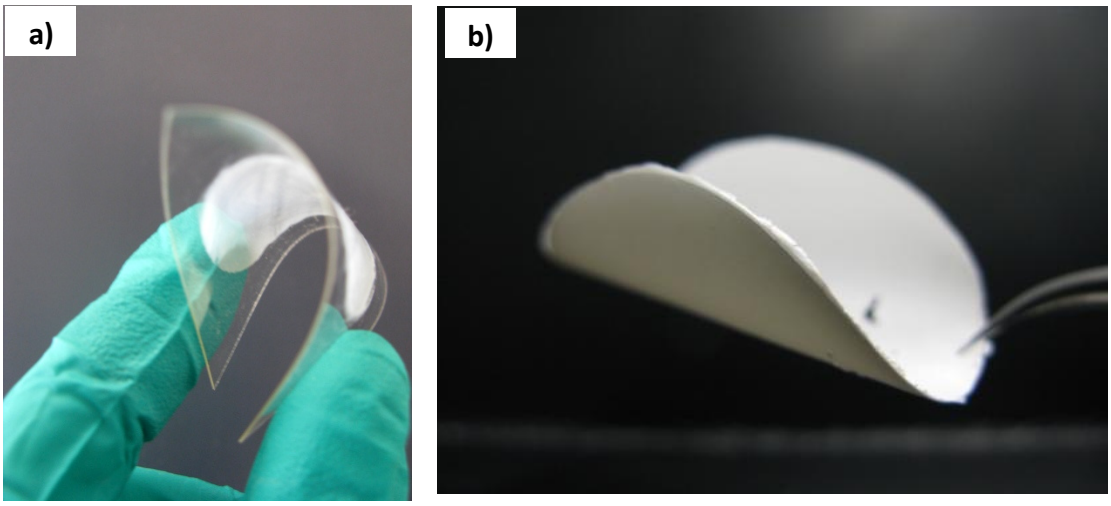

Fig. S4 a) BN membranes prepared from the BN solutions. a) thin layer deposited on PET. b) BN self-standing thick membrane.

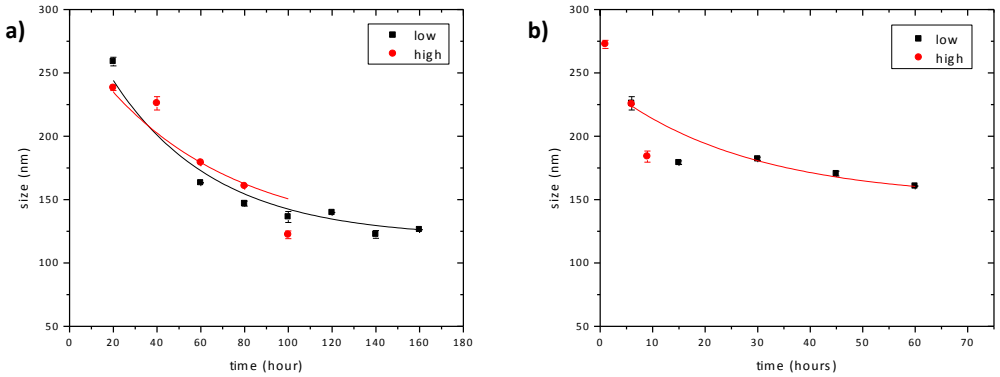

Fig. S5 Evolution of BN nanosheet size exfoliated by ultrasonication and Ball milling measured in solution by DLS. Lines show the corresponding exponential fit of the data.

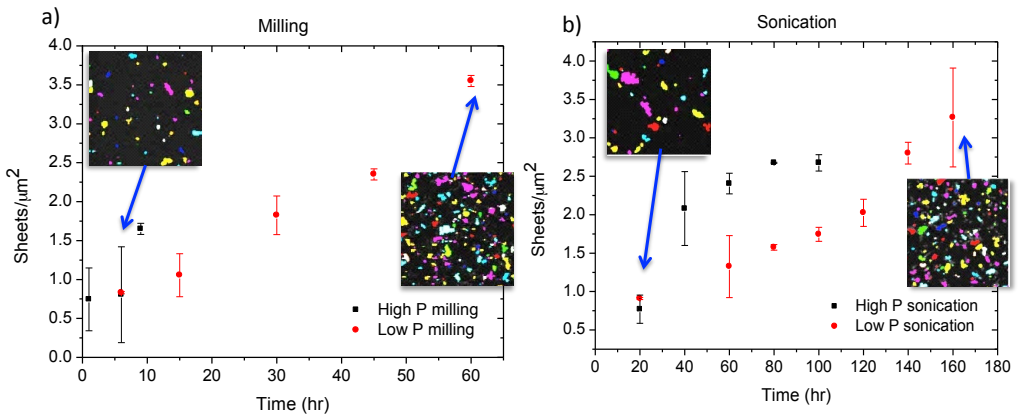

Fig. S6 Graphs representing the number of sheets counted per μm^2 for a) sonication and b) ball milling. Inside the graphs we also show typical processed images from the AFM analysis of the BN samples at lowest or highest concentrations.

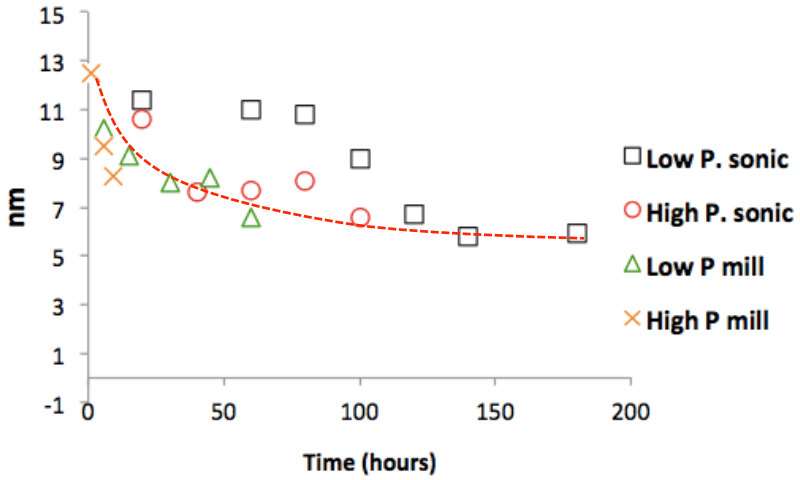

Fig. S7 Evolution of BN nanosheet thickness exfoliated by sonication and Ball milling in solution, measured by AFM. The lines are just a reference for the eye.

Table S1: Statistical distributions

	Equation $f(x)$	Reliability $N(x)$	Mean μ	Variance σ^2
Gaussian	$\frac{1}{w\sqrt{2\pi}} e^{-\frac{(x-x_0)^2}{2w^2}}$	$\frac{1}{2} - \frac{1}{2} erf\left\{\frac{x-x_0}{w\sqrt{2}}\right\}$	x_0	w^2
Log-normal	$\frac{1}{xw\sqrt{2\pi}} e^{-\frac{(\ln x-x_0)^2}{2w^2}}$	$\frac{1}{2} - \frac{1}{2} erf\left\{\frac{\ln x-x_0}{w\sqrt{2}}\right\}$	$e^{x_0+w^2/2}$	$\left(e^{w^2}-1\right)e^{2x_0+w^2}$
Weibull	$\frac{k}{\lambda}\left(\frac{x}{\lambda}\right)^{k-1} \cdot e^{-(x/\lambda)^k}$	$e^{-(x/\lambda)^k}$	$\lambda \cdot \Gamma(1+1/k)$	$\lambda^2 \cdot \Gamma(1+2/k) - \mu^2$
Gamma	$\Gamma(\alpha) x^{\alpha-1} e^{-\beta x}$	$\frac{1}{\Gamma(\alpha)} \gamma(\alpha,\beta x)$	$\frac{\alpha}{\beta}$	$\frac{\alpha}{\beta^2}$

note:

error function: $erf\{z\} = \frac{2}{\sqrt{\pi}} \int_0^z e^{-t^2}\, dt$

lower incomplete Γ function: $\gamma(\alpha,x) = \int_0^x t^{\alpha-1} e^{-t}\, dt$

Table S2: Exfoliation techniques used (see text for more details)

Procedure	High Power	Low Power
Sonication	220 W (effective power)	66 W (effective power)
Ball milling	450 rpm (rotation speed)	200 rpm (rotation speed)

REFERENCES

1 Hennrich, F. *et al*. The mechanism of cavitation-induced scission of single-walled carbon nanotubes. *Journal of Physical Chemistry B* **111**, 1932-1937, (2007).

2 Khan, U. *et al*. Solvent-Exfoliated Graphene at Extremely High Concentration. *Langmuir* **27**, 9077-9082, (2011).

3 Xia, Z. Y. *et al*. The Exfoliation of Graphene in Liquids by Electrochemical, Chemical, and Sonication-Assisted Techniques: A Nanoscale Study. *Advanced Functional Materials*, DOI: 10.1002/adfm.201203686, (2013).

4 Li, L. H. *et al*. Large-scale mechanical peeling of boron nitride nanosheets by low-energy ball milling. *Journal of Materials Chemistry* **21**, 11862-11866, (2011).

5 Coleman, J. N. *et al*. Two-Dimensional Nanosheets Produced by Liquid Exfoliation of Layered Materials. *Science* **331**, 568-571, (2011).

6 Khan, U. *et al*. Size selection of dispersed, exfoliated graphene flakes by controlled centrifugation. *Carbon* **50**, 470-475, (2012).

7 Schlierf, A. *et al*. Nanoscale insight into the exfoliation mechanism of graphene with organic dyes: effect of charge, dipole and molecular structure. *Nanoscale* **5**, 4205-4216, (2013).

8 Yang, H. *et al*. A simple method for graphene production based on exfoliation of graphite in water using 1-pyrenesulfonic acid sodium salt. *Carbon* **53**, 357-365, (2013).

9 Palermo, V. Not a molecule, not a polymer, not a substrate... the many faces of graphene as a chemical platform. *Chemical Communications* **49**, 2848-2857, (2013).

10 Lotya, M., Rakovich, A., Donegan, J. F. & Coleman, J. N. Measuring the lateral size of liquid-exfoliated nanosheets with dynamic light scattering. *Nanotechnology* **24**, #265703, (2013).

11 (Scanning Probe Image Processor, version 2.0000, Image Metrology A/S, Lyngby, Denmark.).

12 Gentile, P. *et al*. STM study of ultra-thin (< 2 nm) silicon oxide. *Journal of Non-Crystalline Solids* **322**, 174-178, (2003).

13 Liscio, A. Scanning Probe Microscopy beyond Imaging: A General Tool for Quantitative Analysis. *ChemPhysChem* **14**, 1283-1292, (2013).

14 Morita, M., Ohmi, T., Hasegawa, E., Kawakami, M. & Ohwada, M. GROWTH OF NATIVE OXIDE ON A SILICON SURFACE. *Journal of Applied Physics* **68**, 1272-1281, (1990).

15 Palermo, V. *et al*. Scanning probe microscopy investigation of self-organized perylenetetracarboxdiimide nanostructures at surfaces: Structural and electronic properties. *Small* **3**, 161-167, (2007).

16 Liscio, A. *et al*. Charge transport in graphene-polythiophene blends as studied by Kelvin Probe Force Microscopy and transistor characterization. *Journal of Materials Chemistry* **21**, 2924-2931, (2011).

17 Los, S. *et al*. Cleavage and size reduction of graphite crystal using ultrasound radiation. *Carbon* **55**, 53-61, (2013).

18 Catheline, A. *et al*. Solutions of fully exfoliated individual graphene flakes in low boiling point solvents. *Soft Matter* **8**, 7882-7887, (2012).

19 Shih, C. J., Lin, S. C., Sharma, R., Strano, M. S. & Blankschtein, D. Understanding the pH-Dependent Behavior of Graphene Oxide Aqueous Solutions: A Comparative Experimental and Molecular Dynamics Simulation Study. *Langmuir* **28**, 235-241, (2012).

20 Marago, O. M. *et al*. Brownian Motion of Graphene. *Acs Nano* **4**, 7515-7523, (2010).

21 Pugno, N. M. The design of self-collapsed super-strong nanotube bundles. *Journal of the Mechanics and Physics of Solids* **58**, 1397-1410, (2010).